SCIENTIFIC REPORTS

OPEN

Quantitative analysis of magnetic spin and orbital moments from an oxidized iron (1 1 0) surface using electron magnetic circular dichroism

Received: 11 January 2015
Accepted: 03 July 2015
Published: 17 August 2015

Thomas Thersleff[1], Jan Rusz[2], Stefano Rubino[1,3], Björgvin Hjörvarsson[2], Yasuo Ito[4], Nestor J. Zaluzec[5] & Klaus Leifer[1]

Understanding the ramifications of reduced crystalline symmetry on magnetic behavior is a critical step in improving our understanding of nanoscale and interfacial magnetism. However, investigations of such effects are often controversial largely due to the challenges inherent in directly correlating nanoscale stoichiometry and structure to magnetic behavior. Here, we describe how to use Transmission Electron Microscope (TEM) to obtain Electron Magnetic Circular Dichroism (EMCD) signals as a function of scattering angle to locally probe the magnetic behavior of thin oxide layers grown on an Fe (1 1 0) surface. Experiments and simulations both reveal a strong dependence of the magnetic orbital to spin ratio on its scattering vector in reciprocal space. We exploit this variation to extract the magnetic properties of the oxide cladding layer, showing that it locally may exhibit an enhanced orbital to spin moment ratio. This finding is supported here by both spatially and angularly resolved EMCD measurements, opening up the way for compelling investigations into how magnetic properties are affected by nanoscale features.

Systems of restricted size and dimensionality represent a frontier for research on magnetic materials. By reducing the spatial dimensions of crystalline magnets, interfacial magnetic properties become more prominent in the overall magnetic behavior of the system[1]. Controlling interfaces through the fabrication of magnetic heterostructures enables researchers to produce materials that exhibit entirely new properties from the bulk constituents alone. For these reasons, considerable research efforts are currently dedicated to improving the understanding of nanoscale magnetic behavior; however, many of the techniques capable of quantifying magnetic moments - such as X-ray Magnetic Circular Dichroism (XMCD) - lack the spatial resolution necessary to directly correlate the magnetic behavior of the material to the nanoscale features from which they arise.

An example of a field where such understanding is necessary is research on magnetic transition metal oxides, particularly the iron oxides. Iron oxides form in a variety of phases exhibiting a wide range of magnetic behavior. Of particular interest is the phase Fe_3O_4, commonly known as magnetite. Magnetite has potential to play a role in the development of nanoscale magnetic applications due to its anticipated

[1]Department of Engineering Sciences, Division of Applied Materials, Uppsala University, Uppsala, Sweden. [2]Department of Physics and Astronomy, Uppsala University, Uppsala, Sweden. [3]Department of Physics, University of Oslo, Oslo, Norway. [4]Department of Physics, Northern Illinois University, DeKalb, IL, USA. [5]Electron Microscopy Center, NanoScience and Technology Division, Argonne National Laboratory, Argonne, IL, USA. Correspondence and requests for materials should be addressed to T.T. (email: thomas.thersleff@angstrom.uu.se) or K.L. (email: klaus.leifer@angstrom.uu.se)

half-metallic behavior[2] leading to a near 100% spin polarization[3,4], high chemical stability in ambient conditions, and ability to stabilize very thin films against the onset of superparamagnetism[5]. It crystallizes in an inverse spinel cubic structure with Fe assuming both +2 and +3 oxidation states in a ferrimagnetic arrangement. Fe^{3+} is evenly distributed among the tetragonal and octahedral sites and is aligned antiparallel while Fe^{2+} is found exclusively on the octahedral site, resulting in a net magnetic moment of nearly $4\,\mu_B$. It is generally considered that the orbital component of this net magnetic moment in bulk magnetite is nearly completely compensated by this symmetry, resulting in a very small net contribution to the total magnetization[6–8]. However, it has been suggested that local structural and chemical variations may break this compensation, increasing its detectable magnitude[9–13]. Since these effects are necessarily nanoscale in origin while the measurement techniques employed probe macroscale materials, it has proven exceedingly difficult to explore these effects in greater detail.

One technique capable of contributing to this effort is Electron Magnetic Circular Dichroism (EMCD) in the Tranmission Electron Microscope (TEM). First proposed in 2003[14] and experimentally demonstrated in 2006[15], EMCD is an exceptionally useful technique for quantifying the magnetic properties of materials on the nanometer scale[16–18] and has been employed in the analysis of magnetic domain walls at the nanoscale[19], Magnetospirillum magnetotacticum[20], polycrystalline magnets[21], LaSr-2 × 4 manganese oxide nanowires[22], CrO_2 thin films[23], Fe_3O_4 nanoparticles[24], and FeCo alloys[25]. It stems from the observation that the electron momentum transfer vector for coherently-scattered phase-shifted electrons is formally equivalent to the photon polarization vector[14,15]. In practice, this means that the sample itself can be used as a beam splitter to break the symmetry of inelastically scattered electrons giving rise to a dichroic effect in the diffraction plane originating from the asymmetry in the density of states inherent to ferromagnetic solids. The conditions for this are optimized when the sample is tilted to either a two-beam[16] or a three-beam[26] condition, although even this is not strictly necessary[27]. The dichroic signal can be extracted by collecting electrons on opposing sides of the systematic row and dispersing them over the ionization edge of interest. This results in acquisition of two independent spectra, typically referred to as "Chiral Plus" and "Chiral Minus," and the EMCD signal itself results from taking their difference[15].

While the high spatial resolution of the EMCD technique clearly distinguishes it from XMCD, there are a number of additional differences that are just beginning to be explored and understood. First, since the EMCD signal depends on the electron channeling conditions of the sample in the TEM, it is possible to use this technique to obtain site-specific magnetic information[28–30]. Second, it has been demonstrated that the magnitude of the EMCD signal (measured as its signal to noise ratio) varies as a function of scattering angle (or q-vector)[26,31–33]. This dependence - known as an "EMCD strength map" - can be experimentally recorded in the TEM either by angularly selecting the inelastically scattered electrons or by energy filtering a series of electron diffraction patterns. When sum rules are applied to the resultant signals, it becomes possible to quantitatively extract the orbital to spin magnetic moment ratio m_L/m_s as a function of q-space[23,26,34–36]. Significantly, while the magnitude of the EMCD signal changes as a function of crystalline symmetry of the magnetic material, the value of m_L/m_s remains invariant for homogeneous systems[26,37].

In this report, we exploit both of these dynamical diffraction properties to extract m_L/m_s for two magnetic materials having the same magnetic species but different crystal structures that overlap in the direction of the electron beam. Such situations readily arise for metallic TEM lamellae prepared in cross section that have been exposed to atmosphere between sample preparation and transfer to the microscope, forming a thin metal oxide layer on the exposed surfaces. If both the film as well as its oxide have a net magnetic moment, two independent, dissimilar EMCD strength maps will be generated. To a good approximation, the total EMCD signal detected at any given q-vector will thus be a linear combination of these EMCD signal maps. Since both EMCD strength maps vary differently in reciprocal space, when sum rules are applied to the entire EMCD signal map, the measured value for m_L/m_s will vary as a function of detector position, which can be experimentally determined with high precision.

We exploit this effect to probe a TEM lamella of bcc iron having an exposed (1 1 0) surface, upon which a thin layer of cubic iron oxide has grown in the {1 1 1} orientation. Based on structure and spectroscopy investigations, we argue that this layer is best described as $Fe_{3-\delta}O_4$ on both exposed surfaces, where δ varies between 0 (yielding mixed valence magnetite, Fe_3O_4) and 0.33 (yielding monovalent maghemite, γ–Fe_2O_3)[9]. By selectively probing different regions in reciprocal space, we show that it is possible to extract magnetic information pertaining to both the underlying iron film as well as its thin oxide surface layer. Our experimental data combined with simulations on the system bring us to the conclusion that these thin $Fe_{3-\delta}O_4$ layers may locally exhibit a large, uncompensated orbital magnetic moment.

Results

Analysis of iron surface oxidation. A film of bcc Fe with a thickness of 50 nm was epitaxially grown on a single crystalline MgO substrate as detailed in the methods section. An initial quality assessment of the film using x-ray diffraction techniques verified a close to single crystal (0 0 1) growth with a Full-Width at Half-Maximum (FWHM) of the rocking curve equal to 0.5°. A thin cross-sectional lamella was subsequently prepared for the TEM using the FIB *in-situ* lift-out method explained in the methods

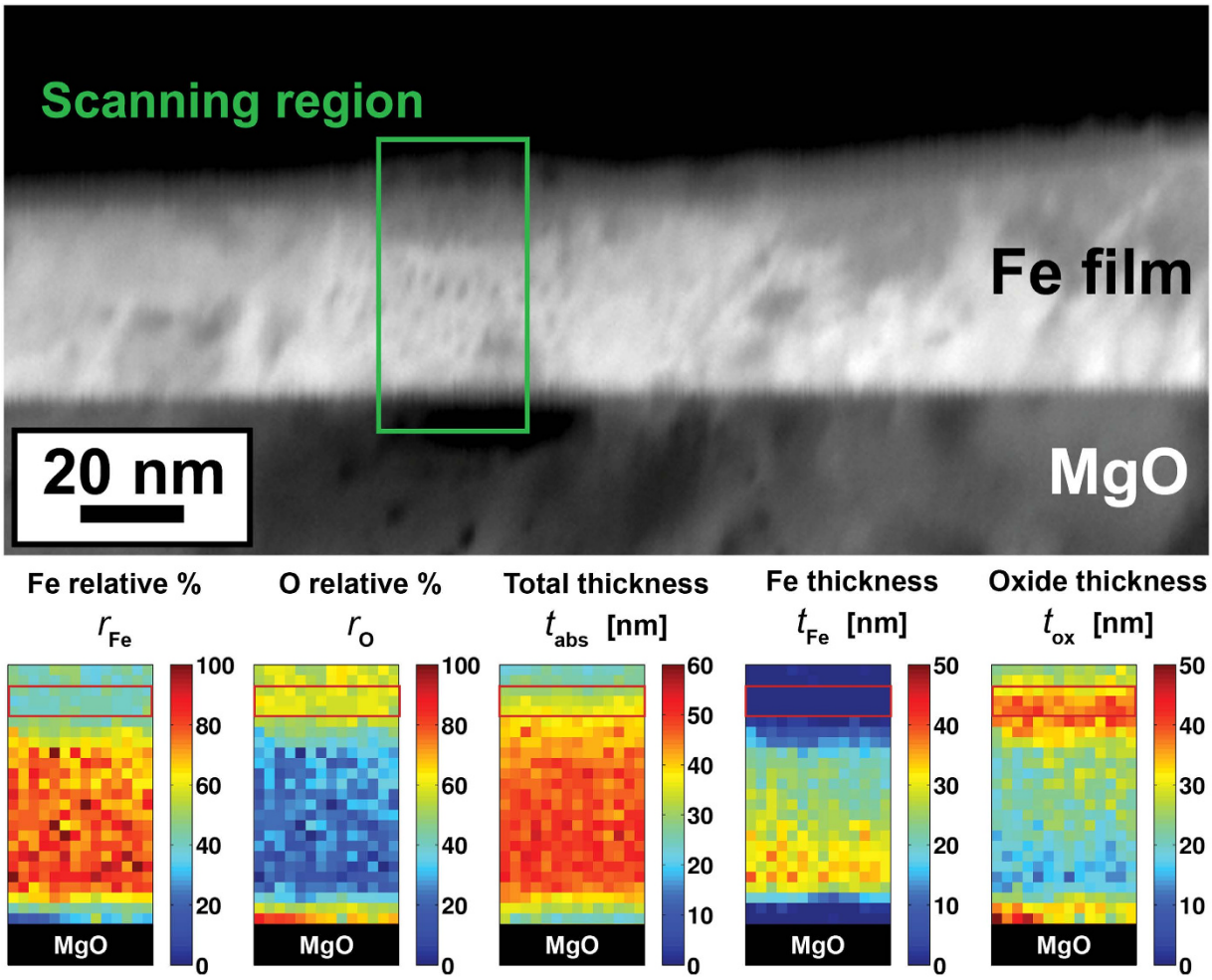

Figure 1. At top, an HAADF survey image denoting the region measured for EMCD is shown. The sub region denoted "surface" contains the largest volume percentage of oxide in the film and its position is marked as a red box on the maps. Relative composition maps for Fe and O extracted from this region are shown in the lower left. Absolute thickness maps for metallic Fe and $Fe_{3-\delta}O_4$ are shown in the lower right. Note that the values for the absolute thickness in the MgO substrate region are blacked out since they cannot be accurately calculated with this method. The pixel size of the maps is approximately 1.5 nm.

section. An overview and structural assessment of the TEM-prepared sample is provided in the supplementary section.

In the thinnest area of the lamella, a region of interest was sought out for the EMCD measurements. A survey image of this region acquired with the microscope in Scanning TEM (STEM) mode using the High Angle Annular Dark Field (HAADF) detector is shown in Fig. 1. The region used for this investigation is depicted in green. The elemental composition of the iron cross-section in this region was investigated with on-axis EELS measurements as described in the methods section. In the lower panel of Fig. 1, real-space maps revealing the relative percentage of both Fe (r_{Fe}) and O (r_o) are presented along with the calculated total absolute thickness (t_{abs}) of the film for any given pixel position. The thickness of both the oxide cladding layers (t_{ox}) as well as the underlying metallic layer (t_{Fe}) was calculated under the assumption of the oxide being structurally similar to Fe_3O_4. See the methods section and the supplementary information for details about the thickness calculation. The on-axis EELS maps reveal that the entire Fe film within the scanned region exhibits a detectable oxygen signal. In the middle of the Fe film, close to the substrate but slightly offset from the interface, oxygen comprises 10–20% of the total atomic concentration. This rises to nearly 60% in the upper region of the film, close to the vacuum. The absolute thickness of the film decreases as a function of distance from the MgO substrate, which is consistent with a wedge shape, as expected from the sample preparation procedure. We therefore conclude that the oxide layer has encapsulated the original iron film and, towards the surface, has consumed nearly all of the metallic iron.

Each pixel position in Fig. 1 contains both an individual EELS spectrum as well as spatial information with a resolution of approximately 1.5 nm. We note that the Bragg scattering angle for the chosen

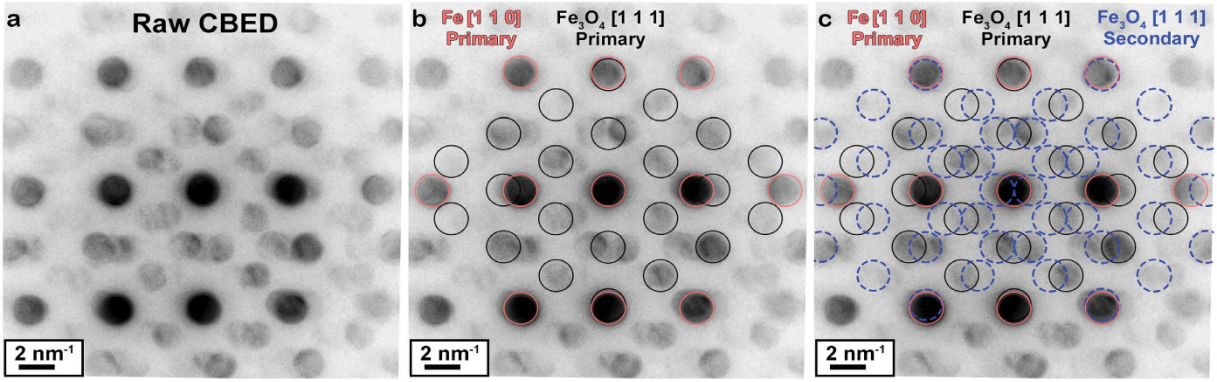

Figure 2. CBED pattern from the scanned region (green box in Fig. 1). Greyscale contrast is inverted to aid visualization in print. In (**a**) the raw pattern is shown. Low order indices for Fe (red) and Fe_3O_4 (black) are provided in (**b**) and secondary reflections arising from the interference mechanism are colored with a dashed blue line in (**c**).

scattering conditions is approximately 13 mrad. Hence, the spreading of the beam through a 50 nm sample thick is only approximately 50 nm 0.013 nm = 0.7 nm, which is much less than the pixel sampling size. This property allows for the EELS data to be spatially segregated into regions corresponding to significant local features. Since the EMCD data were acquired from the same scanning region as the data in Fig. 1, these core-loss EELS data can be used to determine the amount of oxide that contributes to the corresponding EMCD signal. We thus identify two core regions of interest for the EMCD analysis. The first is a summation over all spectra in each spectral image. The second is a summation over the portion of the film with the highest oxide content, denoted the "surface" region. The area of summation is presented in Fig. 1.

The structure of the oxide-encapsulated Fe layer was investigated with both Convergent Beam Electron Diffraction (CBED) and High Resolution TEM (HRTEM) techniques. The CBED pattern is shown in Fig. 2. This pattern was extracted from the middle of the boxed region shown in Fig. 1 and thus reveals the structure of same area used for the EMCD measurements. The most intense reflections can be indexed as Fe [1 1 0], and this is done in Fig. 2b. The additional reflections appear to come in sets of three overlapping discs. The midpoint of these sets of reflections matches well with the indices expected from stoichiometric Fe_3O_4 $[\bar{1}\bar{1}1]$, and these labels are used to index the structure in Fig. 2b. The satellite reflections can be understood as a consequence of dynamical diffraction effects resulting from the propagation of an electron wave through multiple crystalline lattices. This produces an interference lattice that manifests itself as superposition of an additional spatial frequency over all of the primary Bragg reflections. The frequency of this interference lattice Δg is 0.98 nm^{-1} corresponding to $\mathbf{g}_{110}(\mathrm{Fe}) - \mathbf{g}_{4\bar{2}2}(\mathrm{Fe_3O_4})$, and its lower orders are indexed in Fig. 2c. To further refine the structural analysis, High Resolution TEM (HRTEM) experiments were performed on a neighboring region of the film, as displayed in Fig. 3. The lower convergence angle offered by this technique allows for sharper spots in the Fourier transform of HRTEM images than achievable in the CBED pattern. In Fig. 3a, the MgO substrate appears to be monocrystalline but the iron thin film is not. The discrete Fast Fourier Transform (FFT) of this image is shown in Fig. 3b, revealing that both high and low frequencies are present. The lowest order observed spatial frequency $\mathbf{\Delta g}$ is 0.98 nm^{-1}, and this is visible in Fig. 3a as a low frequency "beat" oriented perpendicular to the substrate. This $\mathbf{\Delta g}$ vector can be attributed to an interference phenomenon known as Moiré contrast. The analysis of this phenomena in this manuscript follows the approach described by Amidror[38]. Critically, this approach demonstrates that the best explanation for the oxide structure is the mixed valence $Fe_{3-\delta}O_4$ where δ is close to 0. If δ were close to 0.33 yielding a structure more similar to monovalent γ-Fe_2O_3 or maghemite, then one would expect additional rows of interference reflections due to the reduction of symmetry arising from the presence of cation vacancies needed to maintain charge neutrality[39]. Other iron oxides can be ruled out due to lacking the appropriate lattice plane spacings and symmetry operations to fit with the experimental observations. A more detailed analysis including simulations is provided in the supplementary information. We cannot exclude the possibility that trace amounts of other oxide structures or magnetite with impurities or vacancies may coexist with the $Fe_{3-\delta}O_4$ in our sample. However, these must be present in minute amounts so that they remain undetectable in the HRTEM images and diffraction patterns. As only large volumes of textured crystals can strongly modify the EMCD signal, we would thus expect the influence of any such phases to be negligible.

Thus, based on the EELS, CBED, and HRTEM data, it can be concluded that the lamella is best described as a free-standing trilayer of Fe cladded between two thin $Fe_{3-\delta}O_4$ layers where δ is close to 0. These layers appear to grow with a well-defined texture where Fe [1 1 0] $\|$ $Fe_{3-\delta}O_4$ $[\bar{1}\bar{1}1]$. It is worth noting

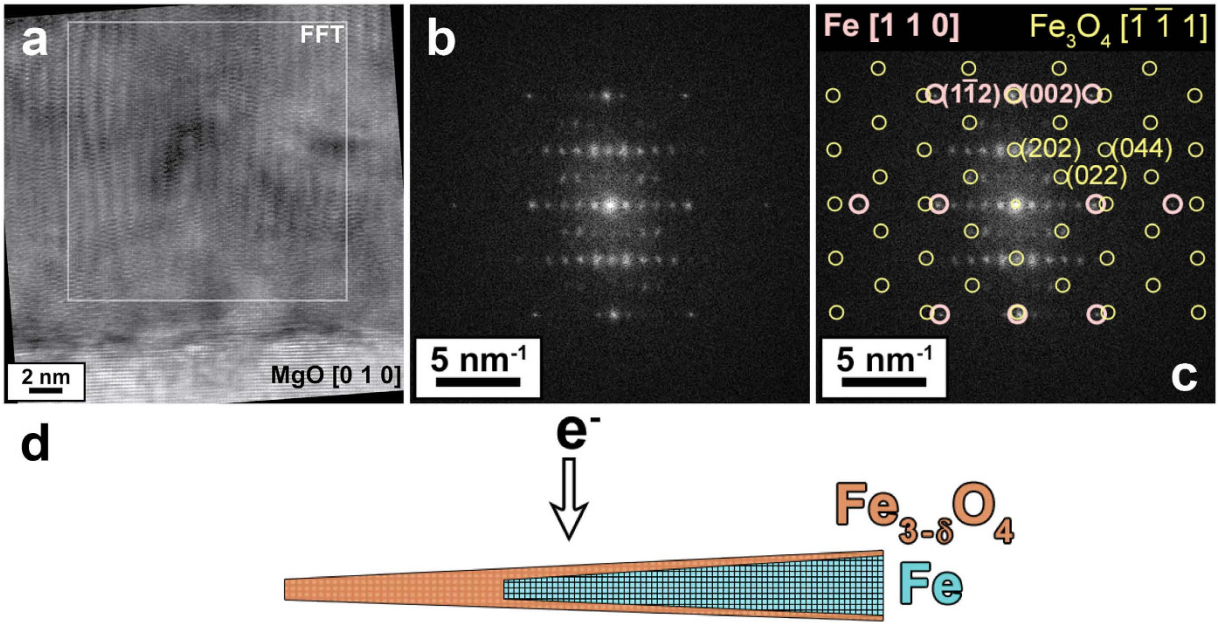

Figure 3. High resolution micrograph of the iron thin film in cross section. In (**a**) the HRTEM image is shown along with a box for the region from which an FFT is taken. The beam is oriented parallel to MgO [0 1 0] and Fe [1 1 0]. In (**b**) the FFT is shown as computed. In (**c**) the FFT is indexed using the first order spatial frequencies for Fe and Fe_3O_4. The unindexed spatial frequencies can be accounted for through convolution of the two materials, as discussed in the supplementary information. This information allows us to construct a structural model for the sample in the TEM, which is presented in (**d**).

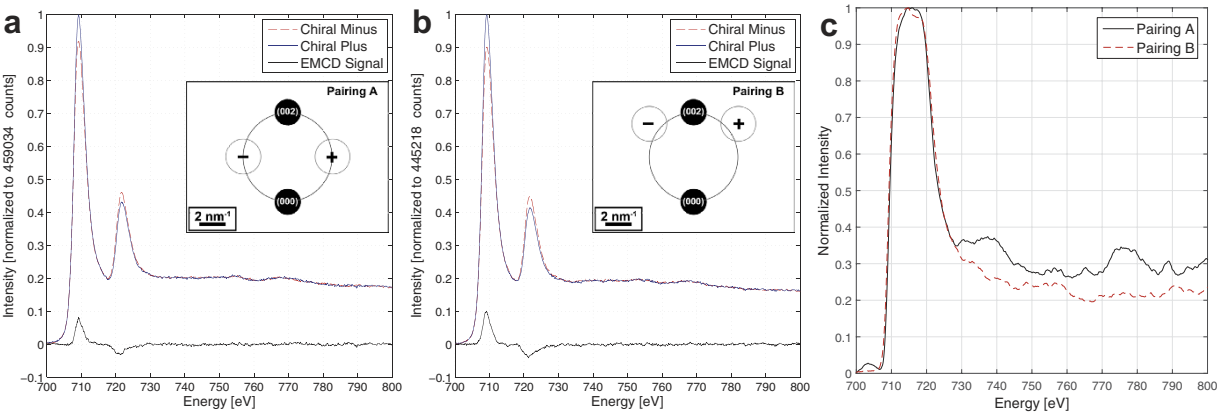

Figure 4. Background subtracted and post-edge normalized EELS spectra for both chiral locations in aperture pairings A (a) and B (b). Both spectra are normalized to the max value of the Chiral Plus spectra and the normalization factor is provided. The difference spectrum (EMCD signal) is also presented. Inset is a schematic depicting the positions of the different aperture pairings in the reciprocal plane. The individual aperture positions are marked + and − to denote Chiral Plus and Chiral Minus, respectively. (**c**) Integral of the EMCD signal for both aperture positions.

that it has been previously shown that $Fe_{3-\delta}O_4$ in this orientation is the most likely oxide to form on an Fe (1 1 0) surface under similar growth conditions[40,41]. A schematic model of this composite structure is presented in Fig. 3d.

EMCD measurements. The EMCD experiments were performed in a two-beam condition with **g** = Fe (0 0 2), as described in the methods section. Two regions of q-space were sampled, and these regions are denoted as aperture pairings A and B throughout the text. Aperture pairing A was located on the Thales circle (Fig. 4a inset), while pairing B was located closer to the Fe (0 0 2) reflection (Fig. 4b inset). Each aperture pairing consisted of two individual aperture positions mirrored about the systematic row, thus

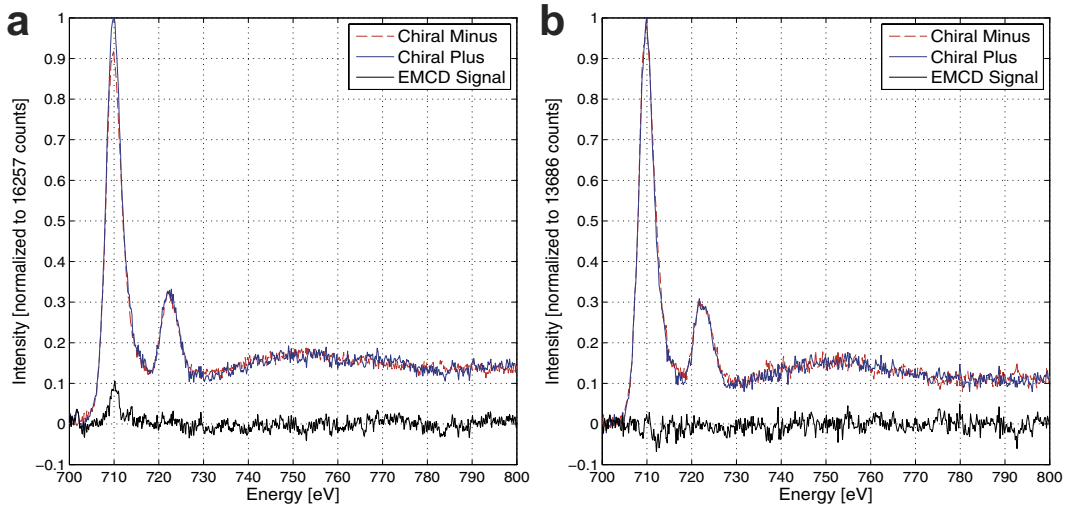

Figure 5. Background subtracted and post-edge normalized EELS spectra for the summation over the "surface" region, as denoted in Fig. 1. Aperture pairings A and B are presented in (**a**,**b**), respectively. The EMCD signals for each chiral pair are also presented.

collecting spectra corresponding to scattering geometries with opposite chirality. These positions are denoted Chiral Plus and Chiral Minus and are defined for each aperture pairing in the insets of Fig. 4a,b.

Figure 4a depicts the two chiral EELS spectra acquired using the scattering geometry of aperture pairing A, while Fig. 4b shows the corresponding spectra collected from aperture pairing B. All spectra in Fig. 4a,b are a summation of all of the individual spectra in their respective spectral image and are plotted on a y-axis that has been normalized to the maximum value of the Chiral Plus spectrum in each pairing to facilitate comparison. In these figures, the plural scattering has been removed[37], the pre-edge background for the Chiral Plus and Chiral Minus spectra has been subtracted, and the signals have been shifted and aligned with respect to each other as described in the methods section. They otherwise represent the raw data. The difference between the two EELS spectra of opposite chirality for each aperture pairing is denominated as the dichroic signal (or "EMCD signal") and is shown along with the spectra on the same normalized scale. The integral of both EMCD signals is presented in Fig. 4c. A clear difference can be seen between the two aperture pairings, indicating that the ratio of the area under the Fe L_2 and Fe L_3 edges changes between aperture pairings. When sum rules are applied to the resulting EMCD signals, the value for m_L/m_s can be extracted as described in the methods section resulting in values of 0.082 ± 0.018 for pairing A and 0.058 ± 0.011 for pairing B. The determination of the error bars is discussed in the supplementary information.

This variation of m_L/m_s in q-space strongly suggests that there are two sources contributing to the measured EMCD signal with dissimilar spin and orbital magnetic components that scatter differently. The presence of two chemically and structurally distinct layers described in the previous section offers a plausible explanation for this effect. To more closely correlate this effect to the different layers, we sum the spectra over the "surface" region denoted in Fig. 1. The results of this summation for aperture pairings A and B are presented in Fig. 5a,b respectively. A striking variation is visible. For aperture pairing A, the asymmetry on the Fe L_3 edge is approximately 10% while on the Fe L_2 edge this asymmetry is below the noise level. This will lead to an increased value of m_L/m_s. This asymmetry nearly vanishes in aperture pairing B, which is additional evidence that the EMCD signal in aperture pairing B is dominated by the metallic iron signal. Such behavior would be expected if the oxide layer is magnetic and exhibits a strong orbital component yet is oriented in such a way that its contribution to the total EMCD signal at aperture pairing B is strongly reduced.

EMCD simulations. To explore potential origins for the observed q-space dependence of m_L/m_s in this composite system, we simulated its inelastic electron scattering behavior. Technical details of the computational approach are provided in the methods section. Figure 6a,b shows the calculated distribution of the magnetic signal originating from the L_3 edge of Fe atoms in the diffraction plane, displayed separately for the iron layer (Fig. 6a) and for the oxide layers (Fig. 6b). This signal corresponds to the energy integral over the Fe-L_3 edge of the difference spectrum between chiral minus and chiral plus positions[36]. It shows that the magnetic signal varies with scattering angles differently for the iron and the oxide layers. This difference, as we discuss below, can qualitatively explain the observed m_L/m_s variation as a function of scattering angles.

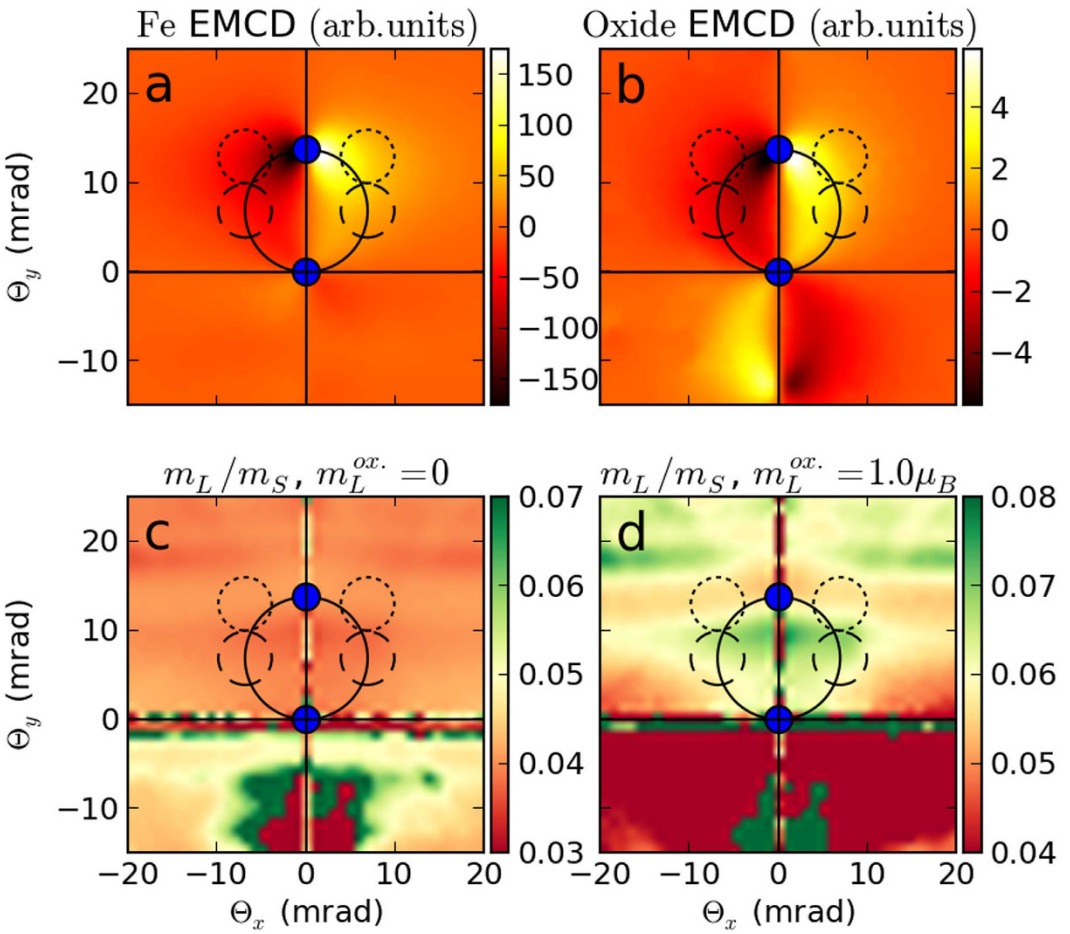

Figure 6. Top row: calculated maps of the EMCD signal at the L_3 edge of iron originating from 30 nm thick bcc Fe (**a**) and two 10 nm thick oxide layers (**b**) as a function of scattering angles Θ_x, Θ_y. Bottom row: maps showing the variation of the resulting m_L/m_s ratio, assuming zero orbital angular momentum in oxide (**c**) or $m_L = 1\mu_B$ (**d**). Blue circles denote positions of the transmitted beam and Bragg-scattered beam G. The Thales circle is drawn with a full line, and aperture pairings A and B are shown with dashed and dotted lines, respectively.

The m_L/m_s ratio in the experiment is determined from the total observed magnetic signal, which can be simulated as a linear combination of the results presented in Fig. 6a,b. When sum rules are applied to the resultant composite map, it becomes possible to calculate the variation of m_L/m_s in reciprocal space, and two such maps are presented in Fig. 6c,d. Despite the much lower strength of the EMCD signal originating from the oxide layer, these maps depend quite strongly on the assumed orbital angular momentum of its iron atoms. Figure 6c shows the variation of m_L/m_s ratio under the assumption of zero angular momentum on Fe atoms in the oxide. In this case, the m_L/m_s ratio varies very weakly within the area where measurements were performed, retaining the expected value of ≈0.043. Stronger variations are observed only along the lines where the EMCD signal originating from bcc Fe is negligible, thus even tiny deviations lead to substantial changes of calculated m_L/m_S ratio. On the other hand, assuming that the iron atoms in the oxide layer have an enhanced orbital moment (for example $m_L = 1\,\mu_B$), the picture changes substantially (Fig. 6d). In the area close to the Thales circle (aperture position A, dashed line) the value is significantly enhanced, while near the region represented by aperture position B (dotted line), the value remains close to the expected 0.043. The range of this variation scales with the size of orbital angular momentum on oxide iron atoms, with smaller values giving rise to less variation. Therefore, based on our simulations, the large variation of m_L/m_s observed in experiment can be explained by the presence of large, unquenched orbital angular momenta on the iron atoms in the oxide layer.

Discussion

The experimental design presented here provides two ways to study magnetic heterostructures that cannot be performed by any other method. First, by exploiting the angular dependency of the EMCD signal through the two different aperture pairings, it is possible to experimentally explore the different magnetic

scattering contributions for both the metallic iron as well as its oxide surface layer. Second, by scanning the probe over a well-defined area from which individual datasets containing both spatial and spectral information are collected, it becomes possible to spatially segregate the EMCD signal with a spatial resolution of approximately 1.5 nm.

By combining both of these methods, we reach the conclusion that the oxide layer is responsible for the measured changes of m_L/m_s. The simplest explanation could be that this is an artifact in the analysis due to the position and width of the interval used for post-edge normalization of the spectra. Particularly, based on discussion of the influence of magnetic EXAFS in XMCD measurements of magnetite[7], it was suggested that the normalization window should start above 760 eV. We do observe that if we shrink the normalization interval to a much smaller width of 10 eV, the calculated value of m_L/m_s becomes more sensitive to the position of normalization interval (see Figure S4a in the supplementary information and the associated discussion). However, note that the post-edge slope is very close to zero both aperture pairings over a wide energy range (see Fig. 4c). As a result, as long as the normalization windows for both pairings are kept the same and their width is large enough to mitigate the influence of noise, pairing A will always have a larger value of m_L/m_s than pairing B. Hence a post-edge normalization artifact can be excluded as the reason for the enhanced m_L/m_s observed in aperture pairing A, and a more detailed analysis of this is presented in the supplementary information.

Thus we are led explore the possibility that the orbital component to the net magnetization in the iron oxide layers is enhanced, as suggested by the simulations. Such results have some precedent in the literature. In the case of γ–Fe_2O_3, Skoropata *et al.* have recently reported a strong increase in the orbital moment for iron in the outer shell of core-shell nanoparticles doped with cobalt[13]. For stoichiometric Fe_3O_4, Huang *et al.* reported orbital moments of $0.67 \pm 0.07\,\mu_B$ at all temperatures measured using XMCD[10], while Li *et al.* inferred a large orbital magnetic moment of $0.51 \pm 0.05\,\mu_B$ at 10 K based on direct observation of the spin moment via Compton scattering and a comparison with literature magnetization data[11]. However, other studies suggest that the orbital moment is quenched within the stoichiometric Fe_3O_4, resulting in a nearly vanishing net value [6–8], and these conflicting reports have lead to some controversy[42,43].

Although our calculations provide strong support for the interpretation suggesting an enhanced orbital angular moment in oxide, we would like to present an alternative argument, which is independent of the simulations. Let's assume that the orbital moments are actually compensated on both iron sublattices and in both iron valencies. The dynamical diffraction effects[25,44] will mix the contributions of the three sublattices in a non-trivial way. A full disentangling of the individual contributions, as performed by Wang *et al.*[30], is beyond the scope and intentions of this manuscript. However, in general, a linear combination of large spin moment contributions will yield a result larger than a corresponding linear combination of the small orbital moment contributions, especially considering that there is a variation of the thickness of the oxide within the studied region. In such case, the observed m_L/m_s ratio would necessarily remain small. But this is in contradiction with our measurements, implying enhancement of the orbital moment in the oxide layer. On the other hand, it is important to point out that the exact value of m_L/m_s ratio for the oxide-dominated pairing A, or extracted from the oxide-rich area, is difficult to interpret without disentangling the individual site contributions[25,30,44]. The reason for the variation of orbital magnetic moments in the literature is not always evident, although a number of theories exist. Kallmayer *et al.* used a monolayer sensitive XMCD technique to probe the interfaces of epitaxially-grown magnetite thin films on MgO and Al_2O_3 substrates[45]. A modest enhancement of the orbital moment was observed at the interface between Fe_3O_4 and Al_2O_3. They interpret this as a consequence of the reduced crystal symmetry of the magnetite at this interface arising from the incorporation of misfit dislocations due to the large lattice mismatch. Another explanation comes from an investigation into the potential for magnetite to harbor large, hidden orbital moments by E. Goering[12]. Goering calculates an average orbital moment of $1.0\,\mu_B$ per Fe atom within magnetite, but that it is nearly completely quenched. He concludes that "slight modifications of the stoichiometry and crystallographic structure [of Magnetite] also give nonvanishing orbital moments." Since the XMCD technique averages over very large areas of crystalline material, however, it is difficult to isolate these effects.

Thus it appears that the observed enhancement of the orbital moment may be partially understood by examining the literature. However, it is critical to emphasize that, due to the unique nature of the EMCD technique presented here, it needs to be considered independently. For example, to the best of our knowledge, all of the quantitative magnetic information on stoichiometric Fe_3O_4 to date comes from bulk systems or thin films where the signals are averaged over regions several hundreds of microns in diameter or more. The results presented here, on the other hand, are a summation of individual spectra acquired from volumes of material illuminated with an electron probe having a diameter of less than 1.5 nm. Thus nanoscale effects may play a greater role than for measurement techniques that probe much larger volumes of material. As an example of how this may manifest itself, we note that it is quite plausible that a series of correlated defects at the interface between Fe and magnetite could lead to a reduction in crystalline symmetry that may account for at least some enhancement of the orbital moment, and that the EMCD technique presented here would be exceptionally sensitive to this. Moreover, although not explicitly investigated in this experiment, the preparation of the lamella with the FIB results in the presence of Gallium impurities on the exposed iron surface. This may influence the growth and magnetic behavior of the cladding oxide layers. For example, Gallium ions have been shown to be soluble

in magnetite and take on a 3+ oxidation state. They substitute for Fe^{3+} at the tetrahedral sites, thereby leading to an enhancement of the net magnetic moment[46]. Although the influence of these impurities on the orbital magnetic moment has not been directly investigated, the suppression of antiferrimagnetic balance of Fe^{3+} ions associated with their introduction may further contribute to the emergence of uncompensated orbital moments.

In conclusion, we present an EMCD-based method that enables the quantitative analysis of magnetic moments in chemically and structurally distinct overlapping magnetic thin films in the TEM with nanoscale spatial resolution. Our structural and chemical analysis of the TEM lamella indicate that the system is best described as a free-standing trilayer of $Fe_{3-\delta}O_4/Fe/Fe_{3-\delta}O_4$ with δ close to zero. By angularly and spatially segregating the EMCD signal, we observe significant variations in the measured value of m_L/m_s which can be correlated to the presence of these oxide layers. Simulations suggest that this can be understood if the orbital component of the net magnetic moment in the oxide is enhanced. Thus this method is capable of providing significant insight into the nature of nanoscale magnetism in a way not yet possible for any other technique.

Methods

Sample Preparation. A thin film of pure iron was deposited by molecular beam epitaxy onto a single crystal (0 0 1) MgO substrate. The sample was prepared for the TEM using the FIB *in-situ* lift-out method[47,48]. A protective bar of a Pt-C compound was locally deposited on the region of interest by decomposing a platinum carbon precursor gas in the presence of electrons accelerated to 3 kV. On top of this, a second bar of approximately 1 μm thickness was deposited by decomposing the same precursor gas in the presence of gallium ions accelerated to 30 kV. A lamella roughly 15 μm in length was milled, extracted, attached to a copper TEM grid using the precursor gas, and thinned to an estimated 100 nm thickness using the 30 kV ion beam. A final polish using a 5 kV gallium ion beam was completed on both sides with an incidence angle of approximately 3° to the lamella face.

Experimental Equipment. The TEM and EELS measurements carried out as part of this study were conducted using a Tecnai F30 (FEI Company) at Uppsala University as well as a Tecnai F20 (FEI Company) at the Argonne National Laboratory Electron Microscopy Center (ANL EMCenter). Both instruments were equipped with Schottky Field Emission guns and operated at 300 kV and 200 kV, respectively. EELS data were acquired on a Tridiem Gatan Image Filter (GIF) (Gatan Inc.). The field emission gun was operated in such a way to produce a high current at the expense of energy resolution, which was close to 1.3 eV, taken as the Full Width Half Max (FWHM) value of the Zero Loss Peak (ZLP). All EELS spectra were acquired with the microscope set in Scanning TEM (STEM) mode with a calibrated camera length of 1877 mm. The minicondenser lens was switched off to yield a lower convergence angle of 1.6 mrad for a fully converged beam, which was diffraction limited by use of the secondary condenser aperture. We estimate that the spatial resolution of this configuration is 1.2 nm. The EELS entrance aperture (physical diameter 1.0 mm) was used to set the collection angle at 2.4 mrad. The aperture was positioned using a script to excite the diffraction shift coils and the exact positions are shown in the insets of Fig. 4a,b as well as in Fig. 6.

In STEM mode, a High Angle Annular Dark Field (HAADF) detector was used to produce a survey image using electrons scattered by angles larger than approximately 30 mrad. This resulted primarily in a mass-thickness contrast mechanism, but also included some diffraction contrast. The region from which all spectrum image data cubes were acquired is shown in green in Fig. 1. A drift correction routine carried out at regular intervals ensured that the probe position within this region could be linked to the survey image and, subsequently, related between all of the individual data cubes. The probe was scanned perpendicular to the Fe/MgO interface with a pixel size of approximately 1.5×1.5 nm.

The EMCD data were acquired by first shifting the aperture to the "Chiral Plus" location of the pairing A shown in the inset of Fig. 4a and recording the electron energy loss range 480–890 eV using an acquisition time of 5 s per pixel and an energy dispersion of 0.2 eV per channel. The aperture position was subsequently shifted to the "Chiral Minus" location and the same region was scanned again. This was repeated for both aperture positions in pairing B (see Fig. 4b, inset). For the core-loss EELS data, the diffraction pattern was shifted on-axis and the acquisition time was reduced to 2 s per pixel. The low-loss region was acquired with the diffraction pattern on-axis using a dispersion of 0.05 eV and an acquisition time of 1×10^{-2} s. Critically, the survey image was not reacquired between aperture shifts, allowing for the same region to be scanned multiple times. Following the acquisition of each individual spectral image, correlated noise was accounted for by taking the average of $3\sqrt{N}$ dark current measurements - where N is the total number of acquisitions - and subsequently subtracted from the gain normalized spectra[49].

Data Treatment. Energy drift in the individual spectra within the spectral images was corrected for by using a cross-correlation algorithm to align the spectra to the Fe L_3 ionization edge within the regions of the film having the largest metallic iron content. The drift correction for the remaining spectra was determined by interpolating a spline fit between the non-corrected regions. For the EMCD spectra, the energy drift correction resulted in a gain averaging over approximately 15 channels, further improving

the signal to noise ratio[50]. Following this step, the effects of plural scattering were removed by deconvolving all of the core-loss spectral images with the on-axis low-loss spectral image[37]. The individual spectra were then summed into two datasets for each aperture position: the whole image and the "surface" region (see Fig. 1). Following the summation, the pre-edge background was removed using a power-law background fit to the region between 670–700 eV[51].

The on-axis core-loss spectral image was used to quantify the relative amount of iron r_{Fe} and oxygen r_{ox} at any given pixel. This was accomplished by fitting the deconvolved data to the differential scattering cross-sections calculated using the Hartree-Slater model as implemented in Digital Micrograph. The effective electron mean free path was then computed for each pixel by utilizing the Fe:O ratio $R = r_{Fe}/r_{ox}$ at that position as proposed by Malis *et al.*[52] and implemented by Egerton in Matlab[51]. This was used to calculate the absolute thickness t_{tot} of the region at each pixel position by using the low-loss spectral image to first extract the relative thickness values. An equation governing the thickness of the oxide layer t_{ox} as a function of R and t_{tot} was derived under the assumption of it being similar in structure to Fe_3O_4. The justification for this assumption is provided in the supplementary information. This yields equation (1)

$$t_{ox} = \frac{t_{tot}\rho_{Fe}}{\frac{4R}{7}\rho_{ox} - \frac{3}{7}\rho_{ox} + \rho_{Fe}}, \tag{1}$$

where ρ_{ox} and ρ_{Fe} are the densities of the oxide and the metallic Fe layers, respectively. t_{Fe} was calculated as t_{abs}–t_{ox}. The primary sources of systematic error for this calculation include the choice of cross-section model and the quantification routine, uncertainty in the local densities of the oxide and metal, the potential presence of an amorphous carbon coating layer, and unknown stoichiometric deviations from pure Fe_3O_4. Since many of these error sources are difficult to quantify, we are not able to provide systematic error bars for this calculation. Despite that, we note that the statistical error appears to be quite low due to the high signal to noise ratio. Consequently, we feel that these data provide a constructive qualitative assessment of the thicknesses of the individual metal and oxide layers.

The EMCD signal was computed by first interpolating the background-removed data to a dispersion of 0.01 eV and then aligning the two spectra of opposite chirality from each aperture pairing along the energy dispersion axis with a cross-correlation algorithm. The post-edge background was subsequently normalized to a window between 745–800 eV and the difference between the spectra was computed. With this, the conditions for sum rules are satisfied and m_L/m_S can be calculated using equation (2)[36],

$$\frac{m_L}{m_S} = \frac{2}{3}\frac{\int_{L3}\Delta I(E)\,dE + \int_{L2}\Delta I(E)\,dE}{\int_{L3}\Delta I(E)\,dE - 2\int_{L2} I(E)\,dE}. \tag{2}$$

The m_L/m_s values in this paper were determined from the difference in the background-removed post-edge normalized data. The integration range for Fe L_3 was 700–718 eV and the integration range for Fe L_2 was 700–800 eV. The uncertainty was estimated by accumulating the errors introduced by counting statistics, background extrapolation, post-edge normalization, and taking the difference between the two chiral spectra. This cumulative error was then propagated through equation (2). More detail is provided in the supplementary information.

We note that this way of processing data, particularly the post-edge normalization step before taking the difference, significantly suppresses the effects of asymmetry of the two beam case[17,44,53]. This follows from the cubic symmetry of both the magnetite and iron layer, which allows to write each ELNES spectrum as a linear combination of nonmagnetic spectrum $N(E)$ and magnetic EMCD part $M_z(E)$[21,37]:

$$\frac{\partial^2\sigma(E,\Omega)}{\partial E\partial\Omega} \propto A(\Omega)N(E) + B(\Omega)M_z(E). \tag{3}$$

The post-edge normalization removes the differences in geometry-dependent coefficients $A(\Omega)$, because EMCD is negligible in the post-edge region. Thus the difference of post-edge normalized spectra faithfully represents the EMCD spectrum.

MATS Simulations. Simulations of the inelastic electron scattering were performed using the classical Bloch-waves method assuming a plane-wave illumination[54–56]. The final summation was done using the mats algorithm[57]; we refer the reader to this paper for further technical details about the evaluation of the dynamical diffraction effects.

Instead of calculating the spectra, we have utilized the method of sum rules inversion, which allows to directly evaluate energy-filtered diffraction patterns for energy intervals corresponding to entire L_3 edge, respectively. This is based on the dipole approximation of the mixed dynamical form-factor, $S(\mathbf{q}, \mathbf{q}', E)$[58], and expressing its L_3 energy integral in terms of ground-state expectation values of local operators, such as number of holes in the $3d$-shell or spin and orbital magnetic moments[36]. Assuming that the magnetization is saturated along the beam-direction (z-direction) and neglecting the anisotropy terms,

which should be negligible for systems of cubic symmetry[53], we obtain the following approximation for the MDFF

$$\int_{L_3} S(\mathbf{q}, \mathbf{q}', E)\mathrm{d}E \propto C_n \mathbf{q}\cdot\mathbf{q}' N_h + iC_m(\mathbf{q}\times\mathbf{q}')_z\left(m_L + \frac{1}{3}m_S\right) \quad (4)$$

where C_n, C_m are scalar coefficients following from the sum rules[34,36] and N_h, m_L, m_s correspond to number of holes in the 3*d* shell and the orbital and spin magnetic moments along the *z*-direction, respectively.

In combination with the MATS algorithm, this approach provides significant speed-up compared to explicit spectral calculations for each scattering angle. More importantly, this method allows for the separate evaluation of the magnetic and non-magnetic signal distributions in the diffraction plane. Since the post-edge normalization can remove the nonmagnetic part of the spectra (see the discussion above), in our simulations we only consider the magnetic part of the signal, which can be obtained by setting $N_h = 0$ in the expression above.

As a structural model, we have separately treated crystalline layers of magnetite and iron, respectively, having orientation and thickness as observed in the experiment. To simulate the bulk iron, we have set $m_s = 1.98\mu_B$ and $m_L = 0.086\mu_B$ as reported by Chen *et al.*[59]. For magnetite layers, we have set spin moments of $m_s = 4.0\mu_B$ for all sublattices, resulting in a net magnetization of $m_s = 4.0\mu_B$. In Fig. 6b,c we assumed zero m_L on both iron sublattices of magnetite, while $m_L = 1\mu_B$ was used for calculation shown in Fig. 6d. The moments on the two iron sublattices of magnetite were oriented ferrimagnetically, assuming that its net magnetic moment is parallel with that of the iron layer.

The resulting maps of the magnetic signal, Fig. 6b,c, contain a scaling factor that takes into account the thickness of each layer and amount of iron atoms per unit volume in iron (84.6 at./nm^3) and magnetite (13.5 and 26.99 at./nm^3), respectively. Note that the resulting magnetic signal strengths have substantially different relative magnitudes, Fig. 6a,b.

We have also performed test calculations comparing plane wave illumination and convergent beam illumination with a 1.6 mrad convergence angle beam in the (0 0 1) zone axis condition for bcc–Fe. This orientation was chosen so that the dynamical diffraction effects are maximized, thus providing an upper limit on the differences that could be expected between the two methods of calculation. However, thanks to Lorentzian broadening of the Bragg spots accompanying the energy-loss events $\Theta_E \approx E/E_0$[51], the resulting diffraction patterns and EMCD signal distribution were very similar. Thus for the multilayer sample, we have only performed simulations assuming plane-wave illumination.

References

1. Gambardella, P. *et al.* Ferromagnetism in one-dimensional monatomic metal chains. *Nature* **416,** 301–304 (2002).
2. Katsnelson, M. I., Irkhin, V. Y., Chioncel, L., Lichtenstein, A. I. & de Groot, R. A. Half-metallic ferromagnets: From band structure to many-body effects. *Rev. Mod. Phys.* **80,** 315–378 (2008).
3. Bibes, M. & Barthelemy, A. Oxide Spintronics. *IEEE Trans. Electron Dev.* **54,** 1003–1023 (2007).
4. Wada, E. *et al.* Efficient spin injection into GaAs quantum well across Fe_3O_4 spin filter. *Appl. Phys. Lett.* **96,** 102510 (2010).
5. Monti, M. *et al.* Magnetism in nanometer-thick magnetite. *Phys. Rev. B* **85,** 020404 (2012).
6. Duffy, J. A. *et al.* Spin and orbital moments in Fe_3O_4. *Phys. Rev. B* **81,** 134424 (2010).
7. Goering, E., Gold, S., Lafkioti, M. & Schütz, G. Vanishing Fe 3d orbital moments in single-crystalline magnetite. *Europhys. Lett.* **73,** 97–103 (2006).
8. Goering, E., Lafkioti, M., Gold, S. & Schuetz, G. Absorption spectroscopy and XMCD at the Verwey transition of Fe_3O_4. *J. Magn. Magn. Mater.* **310,** e249–e251 (2007).
9. Pellegrin, E. *et al.* Characterization of Nanocrystalline γ-Fe_2O_3 with Synchrotron Radiation Techniques. *Phys. Status Solidi B* **215,** 797–801 (1999).
10. Huang, D. J. *et al.* Spin and Orbital Magnetic Moments of Fe_3O_4. *Phys. Rev. Lett.* **93,** 077204 (2004).
11. Li, Y. *et al.* Spin moment over 10-300k and delocalization of magnetic electrons above the Verwey transition in magnetite. *J. Phys. Chem. Solids* **68,** 1556–1560 (2007).
12. Goering, E. Large hidden orbital moments in magnetite. *Phys. Status Solidi B* **248,** 2345–2351 (2011).
13. Skoropata, E. *et al.* Magnetism of iron oxide based core-shell nanoparticles from interface mixing with enhanced spin-orbit coupling. *Phys. Rev. B* **89,** 024410 (2014).
14. Hébert, C. & Schattschneider, P. A proposal for dichroic experiments in the electron microscope. *Ultramicroscopy* **96,** 463–468 (2003).
15. Schattschneider, P. *et al.* Detection of magnetic circular dichroism using a transmission electron microscope. *Nature* **441,** 486–488 (2006).
16. Schattschneider, P. *et al.* Detection of magnetic circular dichroism on the two-nanometer scale. *Phys. Rev. B* **78** (2008).
17. Lidbaum, H. *et al.* Reciprocal and real space maps for EMCD experiments. *Ultramicroscopy* **110,** 1380–1389 (2010).
18. Schattschneider, P. *et al.* Energy loss magnetic chiral dichroism: A new technique for the study of magnetic properties in the electron microscope (invited). *J. Appl. Phys.* **103,** 07D931 (2008).
19. Che, R. C., Liang, C. Y., He, X., Liu, H. H. & Duan, X. F. Characterization of magnetic domain walls using electron magnetic chiral dichroism. *Sci. Technol. Adv. Mat.* **12,** 025004 (2011).
20. Stöger-Pollach, M., Treiber, C., Resch, G., Keays, D. & Ennen, I. EMCD real space maps of Magnetospirillum magnetotacticum. *Micron* **42,** 456–460 (2011).
21. Muto, S. *et al.* Quantitative characterization of nanoscale polycrystalline magnets with electron magnetic circular dichroism. *Nat. Commun.* **5,** 3138 (2014).
22. Carretero-Genevrier, A. *et al.* Chemical synthesis of oriented ferromagnetic LaSr-2 x 4 manganese oxide molecular sieve nanowires. *Chem. Commun.* **48,** 6223 (2012).
23. Loukya, B., Zhang, X., Gupta, A. & Datta, R. Electron magnetic chiral dichroism in CrO2 thin films using monochromatic probe illumination in a transmission electron microscope. *J. Magn. Magn. Mater.* **324,** 3754–3761 (2012).

24. Salafranca, J. *et al.* Surfactant Organic Molecules Restore Magnetism in Metal-Oxide Nanoparticle Surfaces. *Nano Lett.* **12,** 2499–2503 (2012).
25. Warot-Fonrose, B. *et al.* Magnetic properties of FeCo alloys measured by energy-loss magnetic chiral dichroism. *J. Appl. Phys.* **107,** 09D301 (2010).
26. Lidbaum, H. *et al.* Quantitative Magnetic Information from Reciprocal Space Maps in Transmission Electron Microscopy. *Phys. Rev. Lett.* **102,** 037201 (2009).
27. Muto, S., Tatsumi, K. & Rusz, J. Parameter-free extraction of EMCD from an energy-filtered diffraction datacube using multivariate curve resolution. *Ultramicroscopy* **125,** 89–96 (2013).
28. Calmels, L. & Rusz, J. Atomic site sensitivity of the energy loss magnetic chiral dichroic spectra of complex oxides. *J. Appl. Phys.* **109,** 07D328 (2011).
29. Ennen, I. *et al.* Site-specific chirality in magnetic transitions. *J. Magn. Magn. Mater.* **324,** 2723–2726 (2012).
30. Wang, Z. Q., Zhong, X. Y., Yu, R., Cheng, Z. Y. & Zhu, J. Quantitative experimental determination of site-specific magnetic structures by transmitted electrons. *Nat. Commun.* **4,** 1395 (2013).
31. Rubino, S. *et al.* Energy-loss magnetic chiral dichroism (EMCD): Magnetic chiral dichroism in the electron microscope. *J. Mater. Res.* **23,** 2582–2590 (2008).
32. Hébert, C. *et al.* Magnetic circular dichroism in electron energy loss spectrometry. *Ultramicroscopy* **108,** 277–284 (2008).
33. Rubino, S., Schattschneider, P., Rusz, J., Verbeeck, J. & Leifer, K. Simulation of magnetic circular dichroism in the electron microscope. *J. Phys. D: Appl. Phys.* **43,** 474005 (2010).
34. Rusz, J., Eriksson, O., Novák, P. & Oppeneer, P. M. Sum rules for electron energy loss near edge spectra. *Phys. Rev. B* **76,** 060408 (2007).
35. Calmels, L. *et al.* Experimental application of sum rules for electron energy loss magnetic chiral dichroism. *Phys. Rev. B* **76,** 060409 (2007).
36. Rusz, J., Rubino, S., Eriksson, O., Oppeneer, P. & Leifer, K. Local electronic structure information contained in energy-filtered diffraction patterns. *Phys. Rev. B* **84,** 064444 (2011).
37. Rusz, J. *et al.* Influence of plural scattering on the quantitative determination of spin and orbital moments in electron magnetic chiral dichroism measurements. *Phys. Rev. B* **83,** 132402 (2011).
38. Amidror, I. *The theory of the Moiré phenomenon* (Kluwer Academic, Dordrecht, 2009), 2nd edn.
39. Cornell, R. M. *The iron oxides: structure, properties, reactions, occurrences, and uses* (Wiley-VCH, Weinheim, 2003), 2nd edn.
40. Kim, H.-J., Park, J.-H. & Vescovo, E. Fe_3O_4(111)/Fe(110) magnetic bilayer: Electronic and magnetic properties at the surface and interface. *Phys. Rev. B* **61,** 15288–15293 (2000).
41. Kim, H.-J., Park, J.-H. & Vescovo, E. Oxidation of the Fe (110) surface: An Fe_3O_4 (111) / Fe (110) bilayer. *Phys. Rev. B* **61,** 15284–15287 (2000).
42. Goering, E., Lafkioti, M. & Gold, S. Comment on "Spin and Orbital Magnetic Moments of Fe_3O_4". *Phys. Rev. Lett.* **96,** 039701 (2006).
43. Huang, D. J., Lin, H.-J. & Chen, C. T. Reply to comment on "Spin and Orbital Magnetic Moments of Fe_3O_4". *Phys. Rev. Lett.* **96,** 039702 (2006).
44. Song, D., Wang, Z. & Zhu, J. Effect of the asymmetry of dynamical electron diffraction on intensity of acquired EMCD signals. *Ultramicroscopy* **148,** 42–51 (2014).
45. Kallmayer, M. *et al.* Magnetic moment investigations of epitaxial magnetite thin films. *J. Appl. Phys.* **103,** 07D715 (2008).
46. Pool, V. L., Klem, M. T., Chorney, C. L., Arenholz, E. A. & Idzerda, Y. U. Enhanced magnetism of Fe_3O_4 nanoparticles with Ga doping. *J. Appl. Phys.* **109,** 07B529 (2011).
47. Langford, R. M. & Petford-Long, A. K. Preparation of transmission electron microscopy cross-section specimens using focused ion beam milling. *J. Vac. Sci. Technol.* **19,** 2186–2193 (2001).
48. Langford, R. M. & Clinton, C. *In situ* lift-out using a FIB-SEM system. *Micron* **35,** 607–611 (2004).
49. Hou, V.-D. Reduce Correlated Noise in EELS Spectrum with High Quality Dark Reference. *Microsc. Microanal.* **15,** 226–227 (2009).
50. Bosman, M. & Keast, V. J. Optimizing EELS acquisition. *Ultramicroscopy* **108,** 837–846 (2008).
51. Egerton, R. F. *Electron energy-loss spectroscopy in the electron microscope* (Springer, 2011).
52. Malis, T., Cheng, S. C. & Egerton, R. F. EELS log-ratio technique for specimen-thickness measurement in the TEM. J. *Elec. Microsc. Tech*. **8,** 193–200 (1988).
53. Rusz, J., Oppeneer, P., Lidbaum, H., Rubino, S. & Leifer, K. Asymmetry of the two-beam geometry in EMCD experiments. *J. Microsc.* **237,** 465–468 (2010).
54. Saldin, D. K. The theory of electron energy-loss near-edge structure. *Philos. Mag.* **56,** 515–525 (1987).
55. Rossouw, C. J. & Maslen, V. M. Implications of (e, 2e) scattering for inelastic electron diffraction in crystals II. Application of the theory. *Philos. Mag.* **49,** 743–757 (1984).
56. Rusz, J., Rubino, S. & Schattschneider, P. First-principles theory of chiral dichroism in electron microscopy applied to 3d ferromagnets. *Phys. Rev. B* **75,** 214425 (2007).
57. Rusz, J., Muto, S. & Tatsumi, K. New algorithm for efficient Bloch-waves calculations of orientation-sensitive ELNES. *Ultramicroscopy* **125,** 81–88 (2013).
58. Kohl, H. & Rose, H. Theory of Image Formation by Inelastically Scattered Electrons in the Electron Microscope. vol. 65 of *Advances in Electronics and Electron Physics*, 173–227 (Academic Press, 1985).
59. Chen, C. T. *et al.* Experimental Confirmation of the X-Ray Magnetic Circular Dichroism Sum Rules for Iron and Cobalt. *Phys. Rev. Lett*. **75,** 152–155 (1995).

Acknowledgements

The authors acknowledge the STINT research grant (1G2009-2017). In addition, part of this study was accomplished in the Electron Microscopy Center at the Center for Nanoscale Materials of Argonne National Laboratory, a U.S. Department of Energy, Office of Science, Office of Basic Energy Sciences User Facility operated under Contract No. DE-AC02-06CH11357 by UChicago Argonne, LLC. J. R. and K. L. acknowledge the Swedish Research Council. K. L. also acknowledges the Knut and Alice Wallenberg Foundation while J. R. also acknowledges the Göran Gustafsson's Foundation and Swedish National Infrastructure for Computing (NSC center). Special thanks are also due to Paul Thomas at Gatan Inc. for providing the authors with an automated procedure to execute the high quality dark reference correction.

Author Contributions

T.T. designed and executed the experiment, analyzed and interpreted the results, was the main author of the manuscript, and developed the code for quantifying the EMCD spectra. K.L. supervised the experiment and contributed to the writing of the manuscript as well as the analysis of the data. J.R. developed the simulations, interpreted the results, and contributed to the writing of the manuscript. S.R. contributed to the interpretation of the Moiré contrast. B.H. provided the sample and assisted in the conceptualization of the experiment. Y.I. and N.Z. assisted with the experimental design and execution. All authors discussed the results and commented on the manuscript.

Additional Information

Supplementary information accompanies this paper at http://www.nature.com/srep

Competing financial interests: The authors declare no competing financial interests.

How to cite this article: Thersleff, T. *et al.* Quantitative analysis of magnetic spin and orbital moments from an oxidized iron (110) surface using electron magnetic circular dichroism. *Sci. Rep.* **5**, 13012; doi: 10.1038/srep13012 (2015).

SCIENTIFIC REPORTS

OPEN

Erratum: Quantitative analysis of magnetic spin and orbital moments from an oxidized iron (1 1 0) surface using electron magnetic circular dichroism

Thomas Thersleff, Jan Rusz, Stefano Rubino, Björgvin Hjörvarsson, Yasuo Ito, Nestor J. Zaluzec & Klaus Leifer

Scientific Reports **5**:13012; doi: 10.1038/srep13012; published online 17 August 2015; updated on 29 October 2015

In the original version of this Article, Klaus Leifer was incorrectly listed as being affiliated with 'Department of Physics and Astronomy, Uppsala University, Uppsala, Sweden'. The correct affiliation is listed below:

Department of Engineering Sciences, Division of Applied Materials, Uppsala University, Uppsala, Sweden.

This error has now been corrected in both the HTML and PDF versions of the Article.